Journal of Applied Fluid Mechanics, Vol. 10, No. 2, pp. 749-762, 2017.
Available online at www.jafmonline.net, ISSN 1735-3572, EISSN 1735-3645.
DOI: 10.18869/acadpub.jafm.73.239.26632

Flow Simulations with Ultra-Low Reynolds Numbers over Rigid and Flexible Airfoils Subject to Heaving and Flapping Motions

D. Antonelli[1,2†], C. Sacco[3] and J. Tamagno[1]

[1] *Cordoba National University, Cordoba, Cordoba, 5000, Argentina*
[2] *National Scientific and Technical Research Council- CONICET, Argentina*
[3] *Aeronautical University Institute, Cordoba, Cordoba, 5000, Argentina*

†*Corresponding Author Email: dinoantonelli@hotmail.com*

(Received June 3, 2016; accepted November 17, 2016)

ABSTRACT

Numerical simulations of flow patterns at ultra-low Reynolds numbers over rigid and flexible airfoils are presented, and the influence of flexibility on main aerodynamic properties are discussed. Typical unsteady flights like heaving and flapping are, in terms of Reynolds and Strouhal numbers, reduced frequencies and FSI (Fluid Structure Interaction) factor, are valuated. It has been found that for some flexibility levels, the aerodynamic forces and propulsive efficiency are enhanced if compared with a rigid airfoil. The mathematical technical approach used to solve the laminar-incompressible flow equations coupled with structural algorithms, is described.

Keywords: Aerodynamic wing sections; CFD; Fluid structure interaction; Unsteady flows; Low Reynolds; Flexible airfoil; Partitioned method; Finite element method.

NOMENCLATURE

c	chord
$\mathbf{c}$	convective velocity
C_D	drag coefficient
C_L	lift coefficient
C_P	power coefficient
C_T	thrust coefficient
$\overline{cx}$	generic average coefficient
e	structural thickness
E	young modulus
f_h	heaving frequency
f_α	pitching frequency
h_α	heaving half-amplitude
I	Inertial moment
k	reduced frequency, iteration
L	lift
M	Mach number
P	input power
p	fluid pressure
R_e	Reynolds number
U	reference velocity
St	Strouhal number
t	time
T	thrust
$\mathbf{u}$	fluid velocity
$\mathbf{u}_{ms}$	structural mesh velocity
$\mathbf{u}_{mf}$	fluid mesh velocity
$\hat{\mathbf{u}}$	fractionary velocity
w	transversal structural displacement
$\tilde{\mathbf{w}}$	interface displacement
α	angle of attack
α_a	pitching half-amplitude
δ^*	flexibility
δ	tip displacement
Δt	time step
η	propulsive efficiency
μ_s	structural mass per unit length
ρ_f	fluid density
ρ_s	structural density
ρ^*	density ratio
Σ	FSI intensity factor
$\overline{\sigma}$	stress tensor
ϕ_h	test elemental function
χ_α	pitching phase

χ_h	heaving phase
$\tilde{\Psi}_h$	extended Ψ_h functional space
ψ_h	test elemental function
$\tilde{\psi}_h$	test elemental function
ω	relaxation Aitken factor
Ω	analysis domain

1. INTRODUCTION

The importance of ultra-low Reynolds flows is based on technological applications like MAVs (Micro Air Vehicles). They are flying systems with maximum dimensions of 0.15[m] that can lead to revolutionary improvements in remote sensing and information gathering capabilities both in military as well in civilian applications Radmanesh *et al.* (2014). In many cases, an in depth-study of phenomena observed in flight is necessary to obtain maximum propulsion with the highest efficiency.

Because of Reynolds number effects, aerodynamic characteristics such as lift, drag and thrust of flying vehicles change considerably between MAVs and conventional manned air vehicles. In fact, in the nature, birds or insects flap their wings interacting with the surrounding air to generate lift to stay aloft or producing thrust to fly forward. The main powered flights are: heaving and flapping (flights with free stream) and hovering (flight without free stream).

Unsteady aerodynamic mechanisms such as the generation of a leading edge vortex (LEV), wing-wake interaction, and three-dimensional flow features, such as tip vortex-vortex interactions, all significantly affect the aerodynamic force generation. Another remarkable mechanism that the biological flyers seem to be using is the wing flexibility. Studies have been performed to shed light on the interplay between the structural flexibility and the resulting aerodynamic forces.

The most significant researches that can be named are: Guerrero (2008), carried out unsteady aerodynamic studies at ultra-low Reynolds in 2D and 3D configurations built using the NACA 0012 wing section; Combes and Daniel (2005), have shown that a variety of insects exhibit anisotropy in their wing structures based on static response tests.

Experimental and numerical studies of Kang and Shyy (2012) and Kang *et al.* (2011) have shown that the chord-wise flexibility affects the distribution of the resulting aerodynamic forces in lift and thrust directions. For example, if the plate shape undergoes deformation, then the camber of the plate may change leading to an effective geometry modification, which combined with the pitching angle the direction of the net force can be adjusted in favor of the thrust generation.

Zhu (2007) showed numerically that the thrust and the propulsive efficiencies increased more for a plunging chord-wise flexible airfoil in water than immersed in air. Hence it is seen that the flexibility, including the density ratio can be utilized to control resulting aerodynamic forces. However the precise underlying physics of aeroelastic coupling for flapping wings and its applicability to the MAV designs are yet to be understood.

The aerodynamic force generation caused by structural flexibility, is definitely essential to change local behaviors in thrust and propulsive efficiency. Olivier (2010), Heathcote and Gursul (2005), Chandar and Damodaran (2009), Naderi *et al.* (2016) analyzed flexible and rigid airfoils undergoing sinusoidal flapping motion (or combined pitching and heaving) of flexible insect wings under realistic flight conditions such as forward flight and/or rapid maneuvering.

In the present work useful results to describe the behavior of various 2D rigid and elastic geometries at unsteady ultralow Reynolds flows, are presented. The geometric parameter thickness ratio, were changed and its effects evaluated. In addition, the flow features and the impact on main aerodynamic properties are assessed. The behavior of several unsteady flight dynamics like heaving and flap-ping were also analyzed and its aerodynamic properties determined in terms of Strouhal number, heaving and pitching amplitudes, flexibility, etc. The propulsion and lift mechanisms for flapping air-foils, depending of the topology of the wake, the deformation of the geometry and kinematic parameters are analyzed.

2. METHODOLOGY

Ranges of non-dimensional numbers found relevant to unsteady flights of biological "flappers", are also considered valid for MAVs. A characteristic one for flapping motions is the Strouhal number $St = 2 f_h h_a / U$, where f_h is the heaving frequency and ha the half-amplitude of motion. Therefore, the Strouhal number expresses the ratio between the flapping wing velocity and the reference velocity *U*. The reduced frequency given by $k = \pi f_h c / U$ is another parameter that can be interpreted as a measure of unsteadiness comparing the wave length of the flow disturbance to the chord *c*. On the other hand, the fundamental aerodynamic parameters are computed by:

$$C_L(t) = \frac{L(t)}{\frac{1}{2}\rho_f U^2 c} \tag{1}$$

where C_L is the lift coefficient. The thrust coefficient is

$$C_T(t) = -C_D(t) = \frac{T(t)}{\frac{1}{2}\rho_f U^2 c} \tag{2}$$

if $T = -D$. The input power coefficient is

$$C_P(t) = \frac{P(t)}{\frac{1}{2}\rho_f U^3 c} \tag{3}$$

and thrust efficiency is

$$\eta = \frac{\overline{T}U}{\overline{P}} = \frac{\overline{ct}}{\overline{cp}} \tag{4}$$

represents the relation between the input energy and thrust gained energy. $\overline{ct}$ and $\overline{cp}$ are the average thrust and power coefficients respectively, ($\overline{T}$ and are the average thrust and average power inputs respectively).1

The dimensionless parameters related to flexible flapping wing sections problems are, Olivier (2010): the flexibility,

$$\delta^* = \frac{\rho_f (f_h h_a)^2 c^3}{EI} \tag{5}$$

which relates the dynamic pressure with structural stiffness, and the FSI intensity factor defined by

$$\Sigma = \frac{\rho_f h_a}{\rho_s e} \tag{6}$$

which represent the relation between structural inertial forces and aerodynamic pressure. The density ratio is:

$$\rho^* = \frac{\rho_s}{\rho_f} \tag{7}$$

and the kinematics of the moving airfoils are given by the equations:

$$h(t) = h_a \sin(2\pi f_h t + \chi_h) \tag{8}$$

$$\alpha(t) = \alpha_a \sin(2\pi f_\alpha t + \chi_\alpha) \tag{9}$$

where χ_h and χ_α are the phases angles. The center of rotation is located at the leading edge (0% c) in all cases.

2.1 Numerical Methods

A 2D numerical code of fluid-structure interaction was developed in FORTRAN 90 language. The details are here presented.

2.1.1 Fluid Module

The two-dimensional time-dependent Navier-Stokes equations are solved using the finite element method, assuming incompressible-laminar, flow which is justified since the Mach number of a MAV flight is $M << 0.3$ and the Reynolds number $R_e < 10000$. To represent the unsteady flow, the Navier-Stokes equations are solved in a fixed inertial reference frame incorporating a moving mesh with velocity $\mathbf{u}_{mf}$ following the Arbitrary Lagrangian Eulerian (ALE) formulation, Donea and Huerta (2003). Conservation of mass and momentum in a Ω analysis domain with boundaries $\Gamma_u \bigcup \Gamma_\sigma$, and (t_0, t_f) time interval of analysis, are described by:

$$\nabla.\mathbf{u} = 0 \tag{10}$$

$$\frac{\partial \mathbf{u}}{\partial t} + (\mathbf{c}.\nabla)\mathbf{u} + \frac{1}{\rho_f}\nabla p - \nu\nabla^2\mathbf{u} - \mathbf{f}_e = 0 \tag{11}$$

where $\mathbf{u}$ is the two-dimensional flow velocity vector, ρ_f the constant density, ν the kinematic viscosity, p the pressure, fe the external forces and $\mathbf{c} = \mathbf{u} - \mathbf{u}_{mf}$ is the convective velocity that represents the difference between fluid and mesh velocity.

The boundary conditions are:

$$\begin{aligned} &\mathbf{u} = \mathbf{u}_c \quad in\ \Gamma_u \\ &\overline{\sigma}_f.\mathbf{n} = \mathbf{t} \quad in\ \Gamma_\sigma \end{aligned} \tag{12}$$

where $\overline{\sigma}_f$ is the fluid stress tensor and n is the normal vector to the boundary, Fig. 1. The boundary conditions must be met for all $t \in (t_0, t_f)$. Then the initial conditions are:

$$\begin{aligned} &\mathbf{u} = \mathbf{u}_0 \quad in\ t_0 \\ &p = p_0 \quad in\ t_0 \end{aligned} \tag{13}$$

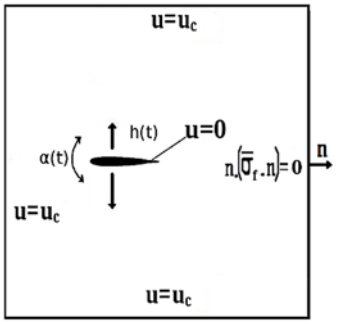

Fig. 1. Boundary conditions in fluid problems.

The equations previously presented can not be solved by a numerical standard form because incompressibility gives rise to a flow field restriction. There are several algorithms to deal with this difficulty and the Fractional Step method used here is one of them. The method meets the LBB condition through the use of same order of approximation for velocity and pressure. In the present work, linear triangular elements are used. For more details see Blasco *et al.* (1995) and Brezzi and Fortin (1991). To apply the Fractional Step algorithm the momentum Eq. (11) is divided in two parts. To simplify the analysis thus mesh velocity is $\mathbf{u}_{mf} = 0$,

$$\hat{\mathbf{u}}^{n+1} = \mathbf{u}^n + \delta t\left[\mathbf{u}^{n+\theta}.\nabla\mathbf{u}^{n+\theta} + \gamma\frac{1}{\rho_f}\nabla p^n + \nu\nabla^n\mathbf{u}^{n+\theta} + \mathbf{f}^{n+\theta}\right] \tag{14}$$

$$\mathbf{u}^{n+1} = \hat{\mathbf{u}}^{n+1} - \frac{\delta t}{\rho_f}(\nabla p^{n+1} - \gamma\nabla p^n) \tag{15}$$

In Eq. (14), the fractionary velocity $\hat{\mathbf{u}}$ is introduced and used in Eq. (15). If the divergence of Eq. (15) is

taken and the continuity equation is applied, results

$$\nabla^2(p^{n+1}-\gamma p^n)=\frac{\rho_f}{\delta t}\nabla.\hat{\mathbf{u}}^{n+1} \tag{16}$$

Through this equation the pressure is calculated. In addition, γ is a numerical parameter such that its values of interest are 0 and 1 and gives the order of approximation. The θ parameter determine the kind of temporal approximation. The values of interest for θ are: θ = 1/2 corresponding to the second or-der scheme of Crank- Nicholson, θ = 1 to backward Euler method (implicit) and θ = 0 corresponding to forward Euler method (explicit).

Then the Finite Element Method is used to discretize the govern equations and it provides an appropriate resolution procedure Lohner (2001). The resultant scheme is of first order (γ = 0) and the temporal discretization (θ = 0) results in Euler for-ward. The test functions $(\psi_h,\phi_h)\in\Psi_h\times\Phi_h$ are used such as:

$$\frac{1}{\delta t}(\hat{\mathbf{u}}_h^{n+1},\psi_h)=\frac{1}{\delta t}(\mathbf{u}_h^n,\psi_h)-(\mathbf{u}_h^n.\nabla\mathbf{u}_h^n,\psi_h)-\nu(\nabla\mathbf{u}_h^n,\nabla\psi_h)-(\mathbf{f}_e^n,\psi_h) \tag{17}$$

$$(\nabla p_h^{n+1},\nabla\phi_h)=\frac{\rho_f}{\delta t}[(\hat{\mathbf{u}}_h^{n+1}-\mathbf{u}_h^n,\nabla\phi_h)-(\nabla\mathbf{u}_h^n,\phi_h)] \tag{18}$$

$$(\mathbf{u}_h^{n+1},\psi_h)=(\hat{\mathbf{u}}_h^n,\psi_h)-\frac{\delta t}{\rho_f}(\nabla p_h^{n+1},\phi_h) \tag{19}$$

where sub index h means it is applied on one element. Ψ_h and Φ_h are functional spaces associated to a partition of the domain Ω called finite element partition Ω_h. The last equations system is semi-implicit because Eqs. (17) and (19) are explicit (lumped mass matrix) and Eq. (18) for the pressure computation is implicit 2.

The discretization of convective terms yields numerical instabilities, therefore stabilization methods must be used. In this work the Orthogonal Subgrid Scale (OSS) algorithm is applied Codina (2000), Principe and Codina (2009). The expression for the convective stabilization term STB_u is:

$$STB_u=\tau_1(\mathbf{u}_h^n.\nabla\mathbf{u}_h^n-\pi_h^n,\mathbf{u}_h^n\nabla\psi_h) \tag{20}$$

where π is the convective term projection and it is defined in Eq. (25). This equation add to momentum Eq. (17) and it is evaluated in t^n, therefore it remains explicit.

The stabilization term of pressure STB_p to be added to the Eq. (18) is:

$$STB_p=-(\tau_2(\nabla p^n-\xi_h^n),\nabla\phi_h) \tag{21}$$

where ξ_h^n is the gradient pressure term projection and it is defined in Eq. (26). In addition, it is evaluated in t^n, therefore it remains explicit.

To present the final complete stabilized scheme, the mesh movement through $\mathbf{u}_m$ is introduced. Then the final scheme of equations results,

$$\frac{1}{\delta t}(\hat{\mathbf{u}}_h^{n+1},\psi_h)=\frac{1}{\delta t}(\mathbf{u}_h^n,\psi_h)-(\mathbf{c}_h^n.\nabla\mathbf{u}_h^n,\psi_h)-\nu(\nabla\mathbf{u}_h^n,\nabla\psi_h)-(\mathbf{f}_e^n,\psi_h)-(\tau_1(\mathbf{c}_h^n.\nabla\mathbf{u}_h^n-\pi_h^n,),\nabla\mathbf{c}_h^n\nabla\psi_h) \tag{22}$$

$$(\nabla p_h^{n+1},\nabla\phi_h)=\frac{\rho_f}{\delta t+\tau_2}[(\hat{\mathbf{u}}_h^{n+1}-\mathbf{u}_h^n,\nabla\phi_h)-(\nabla\mathbf{u}_h^n,\phi_h)]+\frac{\tau_2}{\delta t+\tau_2}(\nabla\xi_h^n,\nabla\phi_h^n) \tag{23}$$

$$(\mathbf{u}_h^{n+1},\psi_h)=(\hat{\mathbf{u}}_h^n,\psi_h)-\frac{\delta t}{\rho_f}(\nabla p_h^{n+1},\phi_h) \tag{24}$$

$$(\pi_h^n,\tilde{\psi}_h)=(\mathbf{c}_h^n.\nabla\mathbf{u}_h^n,\tilde{\psi}_h) \tag{25}$$

$$(\xi_h^n,\tilde{\psi}_h)=(\nabla p_h^n,\tilde{\psi}_h) \tag{26}$$

where $\tilde{\psi}_h\in\tilde{\Psi}_h$ and τ_1,τ_2 are stabilization coefficients. The system of equations of Eqs. (22), (24), (25), (26) are solved in explicit form with lumped mass matrix and the system resultant of Eq. (23) is solved in implicit form through of conjugate gradients with diagonal preconditioner.

Finally the boundary conditions in viscous tensor and velocity are:

- Imposed velocity: $\mathbf{u}=\mathbf{u_c}$
- No slip: $\mathbf{u}=0$
- No traction: $\mathbf{n}.(\bar{\sigma}.\mathbf{n})=0$

In the present work, the algorithm of mesh movement is based in operations of smoothing. The algorithm smooths the mesh in successive iterations after the deformation imposed by the movement of the body with Eqs. (8) and (9). The nodes that are mobile with the kinematics imposed, will be those that are on the surface of the body and be exempt from entering the smoothing of the mesh. Then, the rest of the mesh is smoothed. The algorithm is divided in two parts, the first part consisting of a smoothing rearranges the farthest nodes proper position and the second part, consist of an optimized smoothing more robust, that calculates the metrics of the elements is capable of restoring highly distorted and inverted elements. More details in Canann *et al.* (1998).

2.1.2 Structural Module

The govern equation of the structural model is:

$$\frac{\partial^2}{\partial x^2}\left(EI\frac{\partial w^2}{\partial x^2}\right)=-\mu_s\frac{\partial w^2}{\partial t^2}+q(x) \tag{27}$$

where w is the transverse displacement, μ_s is the

mass per unit length, *E* Young's modulus, *I* inertial moment and *q*(*x*) a distributed transverse load.

Computations done by Kang *et al.* (2011) on a flexible airfoil at higher Reynolds number and for various motion frequencies have shown that a linear Euler-Bernoulli beam model is sufficient for undertaking analysis of the fluid-structure interaction.

The Euler-Bernoulli beam model has been incorporated to solve Eq. (27) using a finite element (FE) representation. The structural damping is not considered in this study and two degree of freedom, i. e. displacement and bending, are allowed at each node. To obtain the solution using the FE Wright and Cooper (2007) is given by the following steps:

- Determine the dynamic properties of each element looking like element stiffness and mass matrices. In order to write the strain energy and the kinetic energy terms for the element, the variation of displacement within the element will need to be expressed as a function of the nodal displacements. It is assumed that the variation of the transverse displacement along the beam elements can be expressed as a cubic polynomial.
- Assemble all the elements to form global mass and stiffness matrices from which modes and responses may be determined. The assembly process satisfies exact compatibility of displacements/rotations between elements. The advantages of the finite element method are that more elements may be used in regions where the displacement and/or stress is expected to vary more rapidly and that more complex geometries and problems may be handled. The general equation to solve is: where Mr is the global mass matrix, w is the displacements vector, Kr is the global stiffness matrix and R represents all the assembled external applied forces. The conformation of R is detailed in the next section.

$$\mathbf{M}_r\ddot{\mathbf{w}} + \mathbf{k_r}\mathbf{w} = \mathbf{R} \tag{28}$$

where $\mathbf{M}_r$ is the global mass matrix, $\mathbf{w}$ is the displacements vector, $\mathbf{k_r}$ is the global stiffness matrix and $\mathbf{R}$ represents all the assembled external applied forces. The conformation of $\mathbf{R}$ is detailed in the next section.

Solve the general eq. (28) via Newmark time integration scheme. In the Newmark method it is supposed that the solution at time step t_n is known for the displacements $\mathbf{w_n}$ and its time derivatives $\dot{\mathbf{w}}_\mathbf{n}$ and $\ddot{\mathbf{w}}_\mathbf{n}$. The semi-discrete equations of motion to be solved at time t_{n+1} are given by

$$\mathbf{M}_r\ddot{\mathbf{w}}_{\mathbf{n+1}} + \mathbf{k_r}\mathbf{w}_{\mathbf{n+1}} = \mathbf{R} \tag{29}$$

and the displacements $\mathbf{w_{n+1}}$ and its time derivative are approximated according to

$$\dot{\mathbf{w}}_{\mathbf{n+1}} = \dot{\mathbf{w}}_\mathbf{n} + \Delta t(1-\gamma_{ne})\ddot{\mathbf{w}}_\mathbf{n} + \Delta t\gamma_{ne}\ddot{\mathbf{w}}_{\mathbf{n+1}} \tag{30}$$

$$\dot{\mathbf{w}}_{\mathbf{n+1}} = \dot{\mathbf{w}}_\mathbf{n} + \Delta t\ddot{\mathbf{w}}_\mathbf{n} + \Delta t^2(1-\beta)\ddot{\mathbf{w}}_\mathbf{n} + \Delta t^2\beta\ddot{\mathbf{w}}_{\mathbf{n+1}} \tag{31}$$

where Δt is the time step size, and γ_{ne} and β are the parameters that determine the stability and accuracy of the scheme. The different values for the parameters γ_{ne} and β originate the Newmark family methods. Stability conditions for the Newmark method implicit schemes are given by

$$\begin{aligned} &\textit{Unconditional} && 2\beta \geq \gamma_{ne} \geq \frac{1}{2} \\ &\textit{Conditional} && \gamma_{ne} \geq \frac{1}{2}, \quad \beta \geq \frac{\gamma_{ne}}{2} \\ &\textit{with} && f_n\Delta t \leq \Omega_{crit} \end{aligned} \tag{32}$$

where Ω_{crit} is the stability condition and f_n is the natural frequency and must be satisfied for each mode in the system. In the present work the "damped" Newmark ($\gamma_{ne} \geq \frac{1}{2}$) scheme is used. This method helps to stabilization of fluid-structure interactions problems Degroote (2010) and Vazquez (2007).

2.13 Coupling Strategy

The fluid-structure interaction is based on a time-domain partitioned solution process, in which the partial differential equations governing the fluid and the structure are solved independently and spatially coupled, through the relations between the fluid and the structure meshes, Degroote (2010). At each time step the fluid F and structural S solvers are called one after the other, until sufficient convergence on the displacements on the shared boundary surface are reached in an inner-iteration before advancing to the next time step.

Since both fluid and structure have been modeled with continuous theory, the treatment of the fluid-solid interface makes no exception. Only mass and momentum conservation equations are considered because no other physical principles are required to describe elastic solid and nearly incompressible flows. Therefore, the momentum and mass conservation at the FSI interface yields the following conditions, Olivier (2010):

$$\begin{aligned} &\mathbf{u}_{ms} = \mathbf{u}_{mf} \\ &\bar{\sigma}_f.\mathbf{n} = \bar{\sigma}_s.\mathbf{n} \end{aligned} \tag{33}$$

where $\mathbf{n}$ is the normal vector to the airfoil. The *f* subindex means fluid and s subindex, structural. The coupling conditions implies that velocities and normal loads, are equals in the intersection of the two mesh. Through the of virtual works principle of aerodynamic forces $\delta W_a = \mathbf{F}_a^T\delta\mathbf{U}_a$ and virtual works principle of structural forces $\delta W_e = \mathbf{F}_e^T\delta\mathbf{U}_e$, the conservation of total energy can be enforced,

$$\delta W_a = \delta W_e \tag{34}$$

The positions of aerodynamic nodes or structural

nodes can be written as reference position $\mathbf{X}_0$ and a relative displacement $\mathbf{U}$ such as $\mathbf{X} = \mathbf{X}_0 + \mathbf{U}$. Therefore, if a $\bar{\mathbf{H}}$ matrix relating the positions of the nodes of the structural mesh $\mathbf{X}_e$ with the nodes of aerodynamic mesh as $\mathbf{X}_a = \bar{\mathbf{H}}\mathbf{X}_e$, then through the Eq. (34) it holds that,

$$\mathbf{F}_e = \bar{\mathbf{H}}^T \mathbf{F}_a \tag{35}$$

In this way, imposition of the conservation of virtual work relates the transfer of kinematic variables from the structural mesh to the aerodynamic mesh, and of forces in the opposite direction, (more de-tails in Maza *et al.* (2012)).

In the code, the coupling conditions are implemented following the method called surface tracking presented in Cebral and Lohner (1997). The surface tracking method suggests that at the be-ginning of the simulation the relative positions between the aerodynamic and structural nodes are determined (matrix $\bar{\mathbf{H}}$). Then, these positions are preserved so that the relative distances between the two meshes does not vary throughout the simulation, and in the other hand, the aerodynamic loads be-come in nodal loads on the structure. The vector of all the assembled external applied forces $\mathbf{R}$ is,

$$\mathbf{R} = \mathbf{F}_e + \mathbf{F}_i = \bar{\mathbf{H}}^T \mathbf{F}_a + \mathbf{F}_i \tag{36}$$

where $\mathbf{F}_i$ are the inertial forces due to the movement.

The coupling between both solvers F and S is implemented through block Gauss-Seidel partitioned method. Starting from known values of fluid structure and mesh in time t_n a scheme of the coupling algorithm is presented in Fig. 2. The Aitken re-laxation parameter is computed with the following equation Vazquez (2007), Kuttler and Wall (2008),

$$\overset{n+1}{k} = -\omega_{k-1}^{n+1} \frac{\left(\mathbf{re}_{k-1}^{n+1}\right)^T \left(\mathbf{re}_k^{n+1} - \mathbf{re}_{k-1}^{n+1}\right)}{\left(\mathbf{re}_k^{n+1} - \mathbf{re}_{k-1}^{n+1}\right)^T \left(\mathbf{re}_k^{n+1} - \mathbf{re}_{k-1}^{n+1}\right)} \tag{37}$$

Where $\mathbf{re}_k^{n+1} = \tilde{\mathbf{w}}_{k+1}^{n+1} - \mathbf{w}_k^{n+1}$ is defined as the residue. The convergence is performed through $\left\|\mathbf{re}_k^{n+1}\right\| \le \varepsilon_0$, where $\left\|\mathbf{re}_k^{n+1}\right\|$ is the residue norm and ε_0 a imposed tolerance.

3. VERIFICATION OF NUMERICAL CODE

3.1 Verification of Baseline Solvers

As a verification case of the fluid solver, a rigid NACA 0012 airfoil in flapping motion is analyzed. The following parameters are considered: pitching and heaving frequencies $f_\alpha = f_h = 0.225Hz$, reduced frequency $k = 0.7096$, maximum heaving half-amplitude $h_a = 1$, phase angle $\chi_a = \pi/2$, Strouhal number $St = 0.45$ and the variable parameter is the pitching half-amplitude α_a.

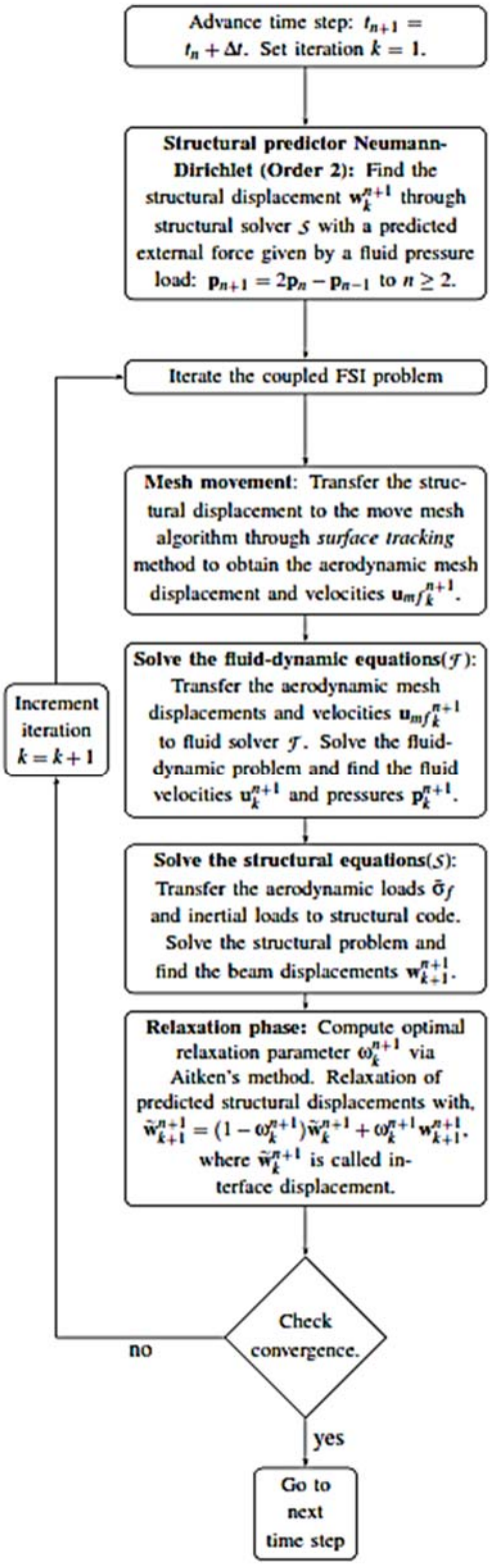

Fig. 2. Chart of fluid-structure interaction coupling algorithm.

In the Table 1 a comparison of maximum lift coefficient C_{Lm} and average thrust coefficient $\bar{ct}$ is

presented. It can be concluded that the results obtained in this work compare well with those given by Pedro *et al.* (2003) and Guerrero (2008).

Table 1 Comparison of average thrust coefficient $\bar{c}t$ and maximum lift coefficient C_{Lm} in flapping motion for rigid NACA 0012

	Pedro et al.		Guerrero		Present Work	
α_a	$\bar{c}t$	C_{Lm}	$\bar{c}t$	C_{Lm}	$\bar{c}t$	C_{Lm}
5°	0.43	8.33	0.42	8.08	0.43	8.21
10°	0.65	7.48	0.66	7.17	0.66	7.24
15°	0.82	6.63	0.84	6.54	0.82	6.39
20°	0.93	5.82	0.94	6.11	1.00	5.51
25°	1.00	5.06	0.96	5.61	1.09	4.99

As a case for validating the solid module, a vibrating cantilever beam model with prefixed displacement is analyzed. This problem were solved by Han *et al.* (1999) with four different theoretical models (Euler-Bernoulli, Shear, Rayleigh and Timoshenko), through the method of eigenfunction expansion.

The beam properties are: length $L = 1m$, tubular section: internal radius $r_i = 0.15m$, external radius $r_e = 0.16m$, section $A = 0.0097389m^2$,

area inertial moment $I = 0.0001171m^4$ and density $\rho_s = 7830kg/m^3$. Twenty finite unidimensional elements along the beam were used. The function of initial transversal displacement $w(x,0)$ is:

$$w(x,0) = (1.667x^3 - 5x^2)10^{-3} \tag{38}$$

where x is the coordinate along beam.

The tip displacements of the beam due to different methods are presented in the Fig. 3. The agreement with the analytic results can be observed.

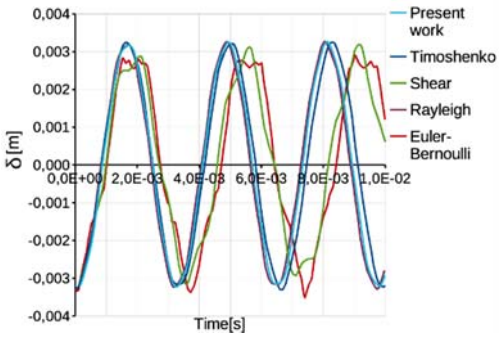

Fig. 3. Comparison of tip displacement of beam with prefixed displacement.

3.2 Verification of FSI Solver

The present FSI solver is verified with a slender flexible structure fixed at the downstream end of a bluff body. The body generates vorticity which induces oscillations in flexible structure. This problem was proposed originally by Wall and Ramm (1998). The domain and boundary conditions are presented in Fig. 4. The material properties of the structure are the density $\rho_s = 0.1Kg/m^3$ and Young modulus $E = 2.5e^6$. The flow properties are the density $\rho_f = 1.18e^{-4}Kg/m.s$, dynamic viscosity $\mu = 1.82e^{-4}Kg/m.s$ and free stream velocity $U = 51.3m/s$. The Reynolds number is $R_e = 333$ with the side length of the square rigid body used like characteristic length $L_b = 1m$. The density ratio is $\rho^* = 84.74$.

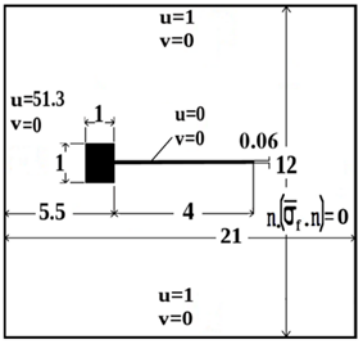

Fig. 4. Problem FSI domain specifications (out of scale).

The fluid-dynamic mesh domain has 24745 elements and the structural mesh has 40 unidimensional elements. The tolerance imposed is ε0 = 3−6. The Fig. 5, shows the periodic states obtained by different authors Wall and Ramm (1998), Kassiotis *et al.* (2011), Vazquez (2007) in comparison with the present work. In this work, the periodic state is assumed when the difference between maximums amplitudes is lower than 0.05. A close agreements are observed between the present computed results and the numerical values of the authors, mentioned above.

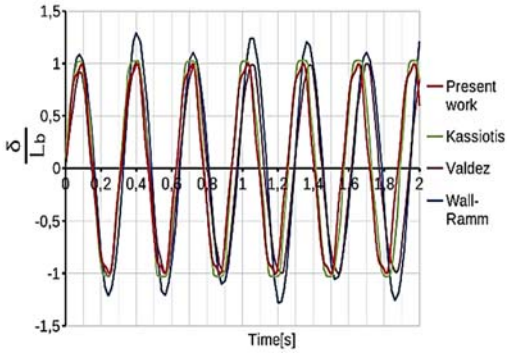

Fig. 5. Comparison of tip displacement of flexible structure fixed at bluff body.

To complete the analysis, in Table 2 a comparison between response frequencies f_{fs} and maximum tip displacements δ with respective errors are listed 3.

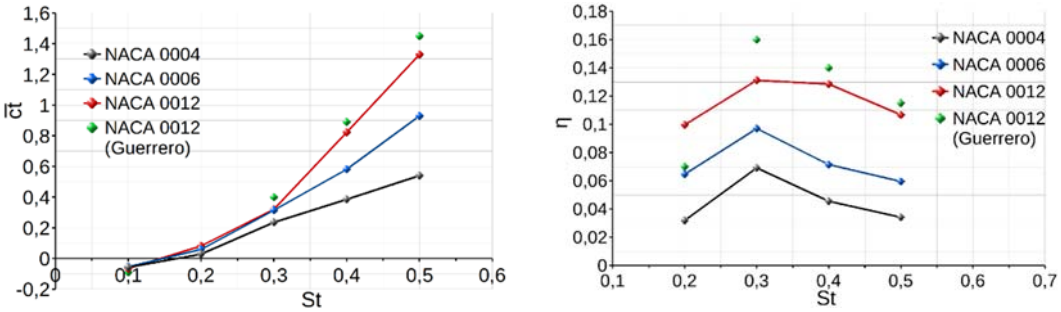

Fig. 6. Average thrust coefficient $\overline{ct}$ and propulsive efficiency η for rigid airfoils in heaving motion (NACA 0004, 0006 and 0012).

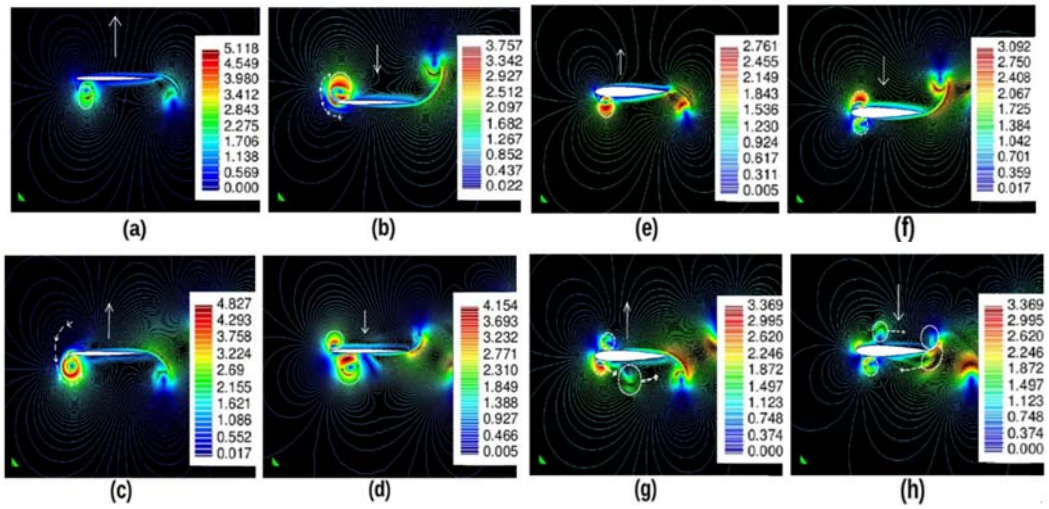

Fig. 7. Velocity contours for rigid NACA 0004 (a, b, c, d) and NACA 0012 (e, f, g, h) in heaving motion (*St* = 0.3).

4. NUMERICAL RESULTS

The fundamental parameter of unsteady analysis is the Strouhal number, defined as $St = 2 f_h f_a / U$. Taylor *et al.* (2003) and Triantafyllou *et al.* (1993) performed a study of wing frequencies and amplitudes, and cruise speeds across a range of birds, in-sects, fishes and cetaceans, to determine Strouhal numbers in "cruising" flight. They found that 75% of the 42 species considered, fall within a narrow range of $0.19 < St < 0.41$ Guerrero (2008). There-fore, a similar range of Strouhal numbers in this work has been selected. The Reynolds number based on the airfoil chord was chosen to be equal to $R_e = 1100$. Which is a representative number of flight regime of insects, small birds and MAVs.

4.1 Heaving Motion of Rigid Airfoils

The first analysis is a heaving motion with kinematic described by Eq. (8). The analysis is applied to NACAs four digits (0004, 0006 and 0012) symmetrical rigid airfoils. The kinematics parameters are: heaving frequency $f_h = 1Hz$ and a variable Strouhal $(0.1 < St < 0.5)$ number throughout the heaving half-amplitude $0.1 < h_a < 0.5$ and $R_e = 1100$. The average thrust coefficient $\overline{ct}$ and propulsive efficiency $\eta = \overline{ct} / \overline{cp}$ in terms of the Strouhal number are presented in Fig. 6. Note that the numerical results obtained by Guerrero (2008) are added. It can be seen in Fig. 6 that thrust and propulsive efficiency increase with airfoil thickness and with the *St*. The maximum efficiency is in $St = 0.3$ in all geometries, and then decrease due to an increase in average input power coefficient $\overline{cp}$.

Comparisons between velocity contours of NACA 0004 and NACA 0012 airfoils at different times Fig. 7, helps to understand the simulation results shown in Fig. 6. Times in Figs. 7 (a) and (e) is $t = 0.45s$, (b) and (f) $t = 0.86s$, (c) and (g) $t = 1.29s$ and (d) and (h) $t = 1.64s$. The formation of leading edge vortex (LEV) and its convection toward the wake, can be detected. With NACA 0004 the LEV remains longer time at the leading edge than it does with NACA 0012. Therefore, the low pressure created there, delays convection of the vortex toward the wake and so, affecting the propulsive and its efficiency.

4.2 Flapping Motion of Rigid Airfoils

The second analysis is the flapping motion. The name flapping is applicable to a combined motion of

heaving and pitching, consequently the kinematics relations given by sinusoidal Eqs. (8) and (9) are simultaneously applied.

In Fig. 8 are shown average thrust coefficients $\overline{ct}$ and propulsive efficiencies η applicable to NACA symmetric rigid airfoils 0004 and 0012, as function of the pitching angle half-amplitude $5^{\circ}<\alpha_a<25^{\circ}$ with $St=0.3$ (maximum efficiency obtained in heaving motion and $f_h=f_\alpha=0.3, h_a=0.5m$). The thrust and efficiency are positives in all cases and greater than obtained in heaving motion of rigid air-foils. The $\overline{ct}$ in NACA 0012 is higher than in NACA 0004 where $\alpha_a<15^{\circ}$ and lower when $\alpha_a>15^{\circ}$. However NACA 0012 is somewhat more efficient than NACA 0004 because average input power $\overline{cp}$ is significantly less in all range of α_a.

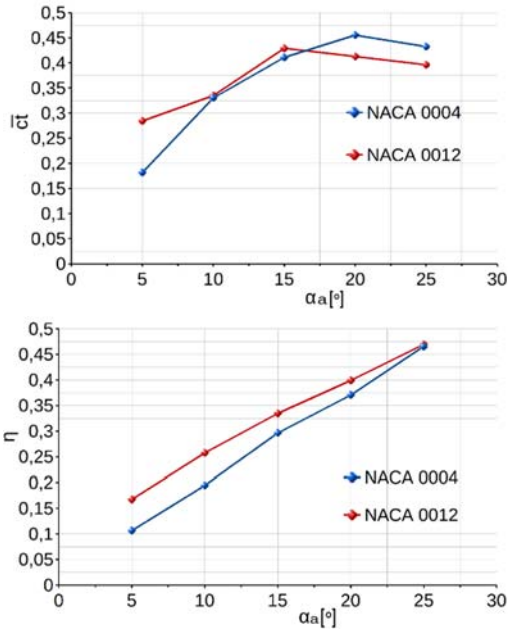

Fig. 8. Average thrust coefficient $\overline{ct}$ and propulsive efficiency η as function of α_a in flapping motion of rigid airfoils (NACA 0004 and 0012).

In Fig. 9 average thrust coefficients $\overline{ct}$ and propulsive efficiencies η applicable to NACA symmetric rigid airfoils 0004 and 0012, as function of the heaving half-amplitude $0.025<h_a<0.5$ $(0.05<St<1)$ are presented. The rest of parameters are $f_h=f_\alpha=1$, $a_\alpha=15^{\circ}$ (in "cruising" flight of small birds, insects was found a range of half-amplitude of pitching $5^{\circ}<\alpha_a<20^{\circ}$) and $\chi_\alpha=\pi/2$. The $\overline{ct}$ coefficient is increased with the heaving amplitude and the difference between the two airfoils is little. The efficiency shows a tendency to increase on values between $0.05<h_a<0.2(St=0.3)$ and then decreases for larger amplitudes. In this case, the thin airfoil is more efficient than thicker airfoil in that region. The pitching amplitude improves the convection of the leading edge vortexes. The con-sequence is an increase of $\overline{ct}$ and η.

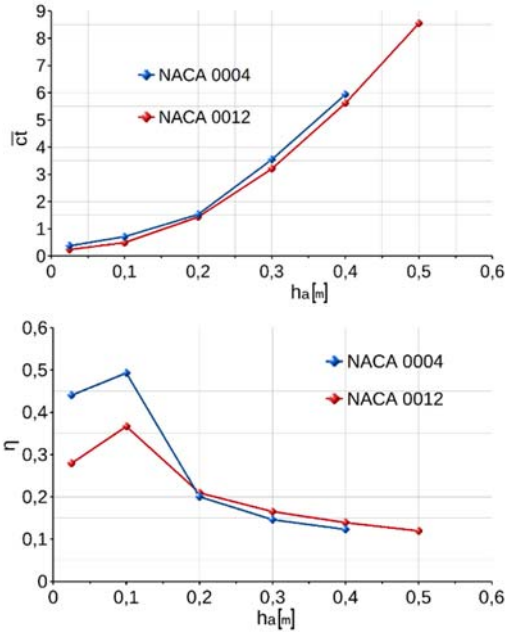

Fig. 9. Average thrust coefficient $\overline{ct}$ and propulsive efficiency η as function of h_a in flapping motion of rigid airfoils (NACA 0004 and 0012).

Table 2 Comparison for FSI problem

	$f_{fs}[1/s]$	$err_f[\%]$	$\delta[m]$	$err_a[\%]$
Present Work	3.19	-	0.99	-
Kassiotis	3.17	0.35	1.03	3.20
Vazquez	3.12	1.94	0.99	0.10
Wall	3.07	3.70	1.33	24.80

4.3 Heaving Motion of Flexible Airfoils

An analysis of the influence of flexibility δ^* (Eq. (5)) and fluid-structure interaction intensity factor $\sum$ in two symmetric airfoils NACA 0012 and NACA 0004 in heaving motion, is performed. The same sinusoidal kinematic and parameters of rigid air-foils are used. The Strouhal number is fixed to $St=0.3$ (maximum efficiency obtained in rigid air-foils) and the Reynolds number $R_e=1100$. The variable parameters through Young modulus E are $8.707e^{-6}<\delta^*<8,707e^{-3}$ and through structural density ρ_s, $0.217<\sum<1.783$. The tolerance of Aitken relaxation imposed in all cases is $\varepsilon_0=10^{-6}$.

The average traction coefficient $\overline{ct}$ and the efficiency η are presented in Figs. 10 (NACA 0012) and 11 (NACA 0004). It can be seen the same behavior in both airfoils, although little higher values for NACA 0004. When the structural flexibility is

lower than $\delta^* = 1e^{-3}$, the coefficients are almost equals to the rigid airfoils (the deformation is very small). When the flexibility $\delta^* > 1e^{-3}$ $\overline{ct}$ increases to a maximum value, due to that the de-formation of the airfoil improves the convection of the leading edge vortexes and increases the intensity of the trailing edge vortexes in both airfoils. That can be observed in a region of flexibility be-tween $1e^{-3} < \delta^* < 1e^{-2}$. Then to $\delta^* > 1e^{-2}$, $\overline{ct}$ decreases due to that high deformation worsens the vortexes convection. If the FSI intensity factor $\sum$ is diminished (structural density ρ_s is increased), $\overline{ct}$ is increased. Note that efficiency η is dependent of $\overline{cp}$, that it presents a high decrease with δ^*.

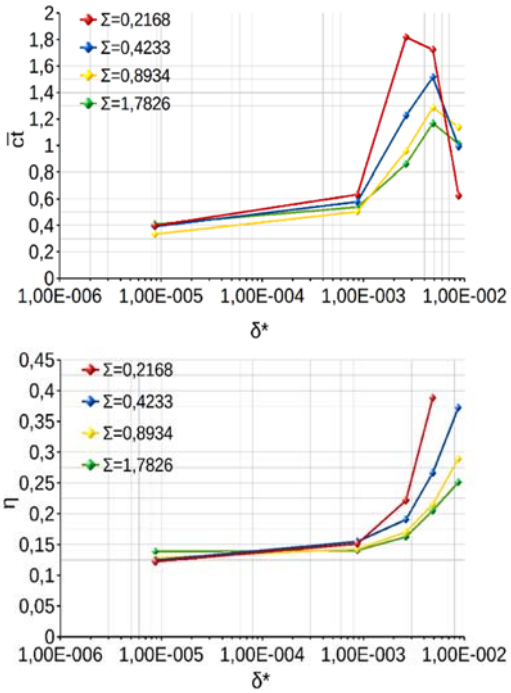

Fig. 10. Average thrust coefficient $\overline{ct}$ and propulsive efficiency η in heaving motion for flexible NACA 0012.

As in the analysis of rigid airfoils, a comparison at different times of velocity contours between flexible NACA 0004 and NACA 0012 (Fig. 12) in de-formed positions helps to understand the results of the simulations. The case selected is $\delta^* = 2,64e^{-3}$ and $\sum = 0,26168$. Times in Fig. 12 are the same used with rigid airfoils. These are (a) and (e) is $t = 0.45s$, (b) and (f) $t = 0.86s$, (c) and (g) $t = 1.29s$, and (d) and (h) $t = 1.64s$. In both airfoils the leading edge vortexes are convected faster than rigid airfoils. A low pressure region is generated in the lower surface during the upstroke and in the up-per surface during the downstroke. In addition, the flexion of airfoil increases the low pressure and improves the convection of LEV toward the trailing edge and its coupling with the wake. The consequence is an increase of $\overline{ct}$ and η like the results are showing.

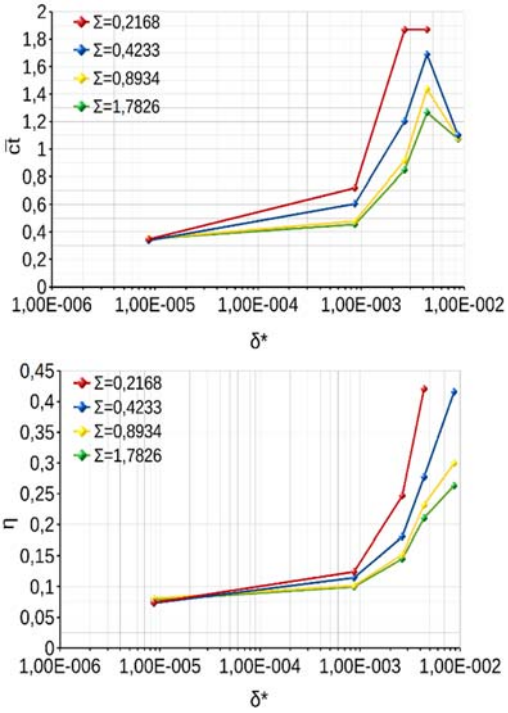

Fig. 11. Average thrust coefficient $\overline{ct}$ and propulsive efficiency η in heaving motion for flexible NACA 0004.

4.4 Flapping Motion of Flexible Airfoils

4.4.1 Sinusoidal kinematic

The next analysis applies to flapping motion on flexible airfoils. The main is determine the influence of the flexibility and FSI factor. The kinematics are sinusoidal and the parameters of motion are $St = 0.3$ $(h_a = 0.15)$, $R_e = 1100$, $f_h = f_\alpha = 1$, $\alpha_a = 10^\circ$, $\chi_\alpha = \pi / 2$. The variable parameters through Young modulus E are $8.707e^{-6} < \delta^* < 8,707e^{-3}$ and through structural density ρ_s, $0.217 < \sum < 1.783$. The tolerance of Aitken re-laxation imposed in all cases is $\varepsilon_0 = 10^{-6}$. It is observed in Figs. 13 and 14 that in both airfoils, $\overline{ct}$ has increased with respect the value obtained in heaving motion due to input of pitching amplitude. Then, the maximum $\overline{ct}$ from flapping are limited to the interval of flexibility $1e^{-3} < \delta^* < 1e^{-2}$, and this interval is the same for maximum $\overline{ct}$ produced in heaving motion. The flexibility helps to improve the obtained propulsion, but not in the magnitude like does in heaving motion.

Note that greater $\overline{ct}$ values are for minimum $\sum$ or higher ρ_s values. If the efficiency η is compared with the results obtained in flexible airfoils in heaving motion, the difference found between maximums values of $\overline{ct}$ are not of big magnitude, it can be concluded that in certain cases the structural flexibility can replace rotations mechanism in MAVs, saving some weight of construction.

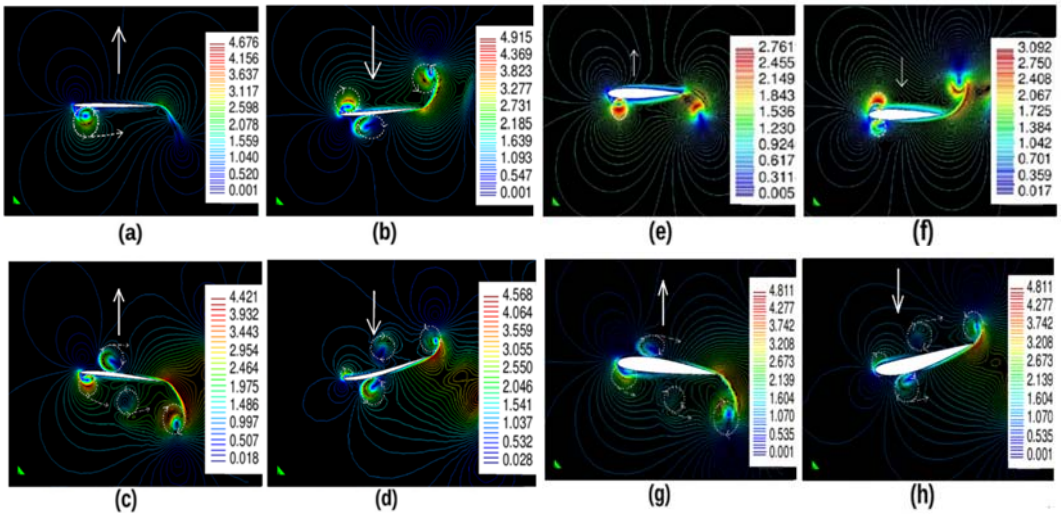

Fig. 12. Velocity contours for flexible NACA 0004 (a, b, c, d) and NACA 0012 (e, f, g, h) in heaving.

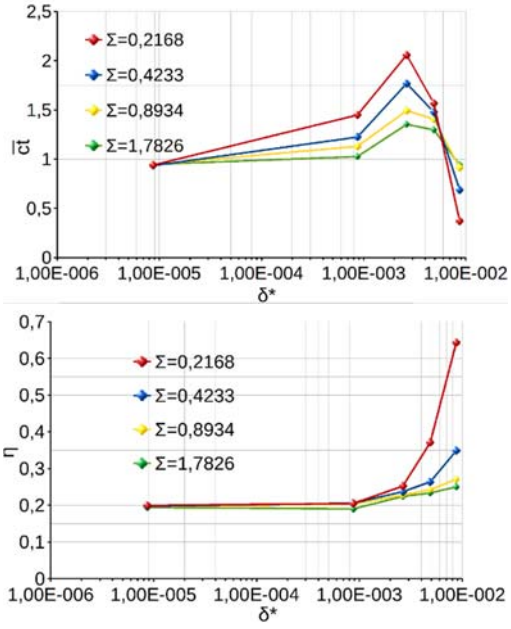

Fig. 13. Average thrust coefficient $\overline{ct}$ and propulsive efficiency η in flapping motion for flexible NACA 0012.

4.4.2 Alternative Kinematic

A third analysis of flexible airfoils in flapping motion with an alternative kinematic is performed. This kinematics is characterized by Eqs. (39):

$$h(t) = \frac{h_a}{\sin^{-1}(0.8)} \sin^{-1}(0.8\sin(2\pi f_h t))$$
$$\alpha(t) = \frac{h_a}{\sin^{-1}(0.8)} \tanh^{-1}(3\sin(2\pi f_\alpha t + \chi_\alpha)) \quad (39)$$

The model takes the wing kinematic used in the Robofly model of Dickinson *et al.* (2004). Based on observation of true insect flights, it was accepted that the wing maintains a constant velocity and angle of attack during most of the stroke, with a relatively strong linear and angular acceleration during stroke reversal. This results with typical "saw-tooth" displacement and "trapezoidal" angle of at-tack pattern of the Robofly kinematic model, are illustrated in Fig. 15. The parameters of kinematic

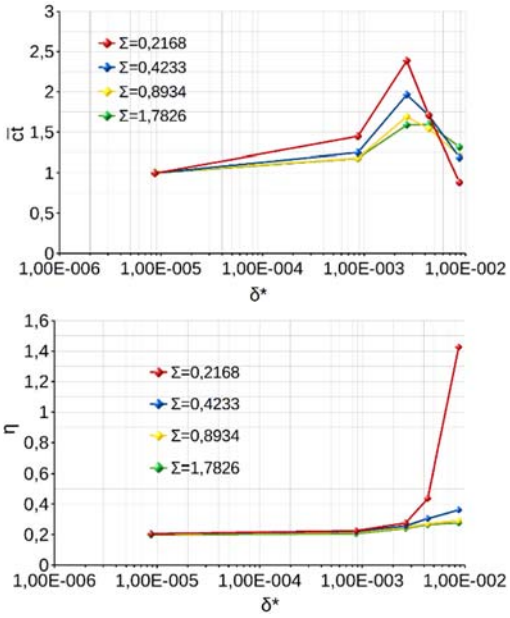

Fig. 14. Average thrust coefficient $\overline{ct}$ and propulsive efficiency η in flapping motion for flexible NACA 0004.

are the same used in sinusoidal kinematic, $St = 0.3(h_a = 0.15)$, $f_h = f_\alpha = 1$, $\alpha_a = 10^\circ$ and $\chi_\alpha = \pi / 2$.

In the Figs. 16 and 17 the average thrust $\overline{ct}$, propulsive efficiency η and power coefficient $\overline{cp}$ are presented. In both airfoils an increase in the thrust

respect to the sinusoidal kinematic is detected. The maximum values are between $1e^{-4}<\delta^{*}<1e^{-3}$. The greater $\overline{ct}$ values (minimum Σ) are given by the NACA 0004 airfoil. In the alternative kinematic, the angle of attack remains in its position of maximum amplitude for longer time, because of its "trapezoidal" pattern (Fig. 15). This implies that vortexes generated at the trailing edge (TEV) are more intense, as a results high speed there is in the wake. Therefore, in the leading edge exist a high suction during more time in comparison with sinusoidal kinematic which allows better convection of generated (LEV). Since both edges in NACA 0004 are sharper than in NACA 0012, the convection is even more intense.

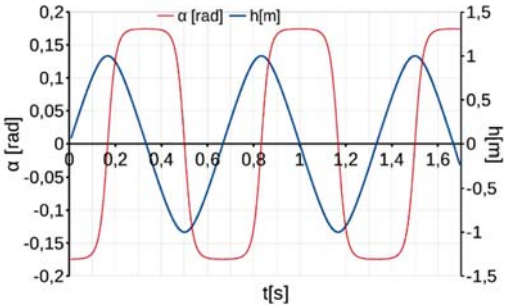

Fig. 15. Alternative kinematic.

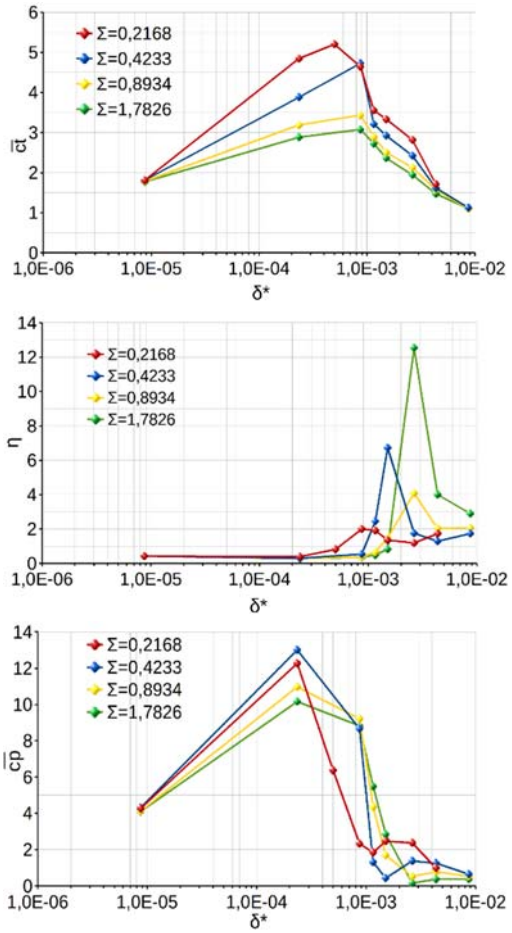

Fig. 16. $\overline{ct}$, $\overline{cp}$ and η coefficients in alternative flapping kinematic (NACA 0004).

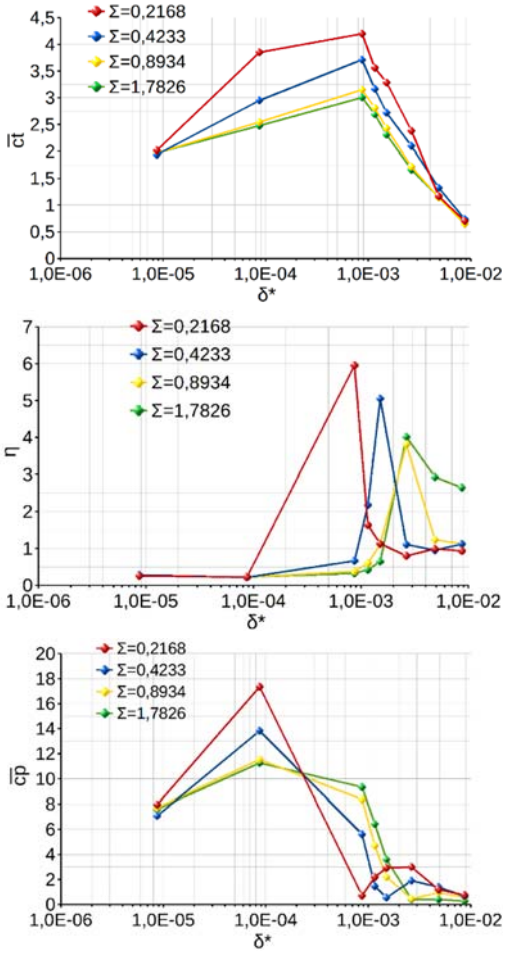

Fig. 17. $\overline{ct}$, $\overline{cp}$ and η coefficients in alternative flapping kinematic (NACA 0012).

The propulsive efficiency presents a different behavior respect to the sinusoidal kinematics and the maximums values are between $1e^{-4}<\delta^{*}<5e^{-3}$. The values of η depend of average power coefficient $\overline{cp}$

5. CONCLUSIONS

In heaving motion studies, rigid and flexible symmetrical wing sections are considered. Average thrust coefficients and propulsive efficiencies for selected motion frequencies are numerically simulated, and the results plotted in terms of a Strouhal number determined using the heaving amplitude and different thickness of NACA symmetric air-foils was studied. As a help to better understand the simulation results, velocity contour pictures al-lowing comparison between wing sections at pre-scribed identical times, are built and shown. Based on these pictures, generation and displacement of vortexes as the wing section executes the heaving motion are described, and justifications about why an airfoil has better performances than other one when executing such motion, are given. In rigid airfoils, it was found that the thicker airfoils have better performance than thinner airfoils. Then, studies related to the influence of flexibility and FSI intensity factor on thrust

coefficients and propulsive efficiencies in heaving motions, are made. From comparisons with rigid data it is concluded that for some flexibility values, improvements are feasible.

Combinations of pitching and heaving motions (flapping) for rigid and flexible wing sections, have also been simulated. The maximum pitch angle and vertical displacement amplitudes are taken as plotting variables. In the rigid airfoils analysis it is found that for given pitch angles a maximum propulsion value exist and increase the thickness improves the performances. Other analysis has shown a increase in propulsion when the heaving amplitude is increased. With flexible airfoils, a comparison between two flapping kinematics is performed. In both kinematics, the influence of flexibility and FSI intensity factor on propulsion and its efficiency are studied. The alternative kinematics shows a improvement of the performance respect of the sinusoidal kinematics. Between the sinusoidal kinematic and heaving motion, a similar behavior is found. Therefore, the possibility exist of somehow using wing flexibility (passive pitching) to replace pitching motion hardware in MAV applications and so, the weight can be reduced.

The Finite Element software here used can in run time, build moving grids needed to perform numerical simulations of unsteady motions like heaving and flapping with rigid as well as with flexible 2D wing sections. For dealing with flexible wing sections, an appropriate structural module and algorithms to compute fluid-structure interactions (FSI), are implemented. In addition, and to handle complex geometries, more elements are created in regions where it is expected that displacements and/or strains vary rapidly.

ACKNOWLEDGMENTS

To CONICET and Aeronautical department of UNC for the financial and facilities support to this research.

REFERENCES

Blasco, J., R. Codina and A. Huerta (1995). A fractional-step method for the incompressible navier stokes-equations related to a predictor-multicorrector algorithm. CIMNE (63).

Brezzi, F. and M. Fortin (1991). Mixed and Hybrid finite element methods. Series in Computational Mechanics 15. Springer-Verlag.

Canann, S. A., J. R. Tristano and M. L. Staten (1998). An approach to combined laplacian and optimization-based smoothing for triangular, quadrilateral, and quad-dominant meshes. International Meshing Roundtable.

Cebral, J. and R. Lohner (1997). Conservative load projection and tracking for fluid-structure problems. *AIAA Journal* 35(4), 687-692.

Chandar, D. D. J. and M. Damodaran (2009). Computational fluid-structure interaction of a flapping wing in free flight using overlap-ping grids. *AIAA.*

Codina, R. (2000). Pressure stability in fractional step element methods for incompressible flows. *Computational Physics* 170(1), 112-140.

Combes, S. A. and T. L. Daniel (2005). Flexural stiffness in insect wings: effect of wins venation and stiffness distribution on passive bending. *American entomologist* 51(1), 42-44.

Degroote, J. (2010). *Development of Algorithms for the Partitioned Simulation of Strongly Coupled Fluid-Structure Interaction Problems*. Ph. D. thesis, Ghent University, Ghent, Belgium.

Dickinson, M. H., F. Lehmann and S. P. Sane (2004). Wing rotation and the aerodynamic basis of insect flight. Science 284(5422), 1954-1960.

Donea, J. and A. Huerta (2003). *Finite Element Methods for Flow Problems*. John Wiley and Sons.

Guerrero, J. (2008). *Numerical Simulation of the Unsteady Aerodynamics of Flapping Flight.* Ph. D. thesis, University of Genova, Genova, Italy.

Han, S. M., H. Benaroya and T. Wei (1999). Dynamics of transversely vibrating beams using four engineering theories. Journal of Sound and vibration 225(5), 935-988.

Heathcote, S. and I. Gursul (2005). Flexible flapping airfoil propulsion at low Reynolds numbers. *AIAA Paper* 2005-1405-CP.

Kang, C. and W. Shyy (2012). Effects of flexibility on the aerodynamics of a hovering flexible airfoil at Reynolds number of 100 to 1000. AIAA Aerospace Sciences Meeting including the New Horizons Forum and Aerospace Ex-position.

Kang, C., H. Aono, C. E. S. Cesnik and W. Shyy (2011). Effects of flexibility on the aerody-namic performance of flapping wings. In *Proceeding of 6th AIAA Theoretical Fluid Mechanics Conference.*

Kassiotis, C., A. Ibrahimbegovic, R. Niekamp and H. Matthies (2011). Nonlinear fluid-structure interaction problem. part i: implicit partitioned algorithm, nonlinear stability proof and validation examples. HAL archives-ouvertes.fr.

Kuttler, U. and W. Wall (2008). Fixed-point fluid-structure interaction solvers with dynamic relaxation. Computational Mechanics, 43(1), 61-72.

Lohner, R. (2001). *Applied CFD Techniques.* John Wiley and Sons.

Maza, M., F. Flores and S. Preidikman (2012). Unsteady and non-linear fluid-structure interaction using potential flow and beam structures. Argentine Association of Computational Mechanics XXXI, 771–795.

Naderi, A., M. Mojtahedpoor and A. Beiki (2016). Numerical investigation of non-stationary

parameters on effective phenomena of a pitching airfoil at low Reynolds number. *Journal of Applied Fluid Mechanics* 9(2), 643–651.

Olivier, M. (2010). *A Fluid-Structure Interaction Partitioned Algorithm Applied to Flexible Flapping Wing Propulsion*. Ph. D. thesis, Universit Laval, Qubec, Canada.

Pedro, G., A. Suleman and N. Djilali (2003). A numerical study of the propulsive efficiency of a flapping hydrofoil. *International Journal for numerical methods in fluids* 42(5), 493-526

Principe, J. and R. Codina (2009). On the stabilization parameter in the subgrid scale approximation of scalar convection-diffusion-reaction equations on distorted meshes. *International Center for Numerical Methods in Engineering*.

Radmanesh, M., O. Nematollahi, M. Nili-Ahmadabadi and M. Hassanalian (2014). A novel strategy for designing and manufacturing a fixed wing MAV for the purpose of increasing maneuverability and stability in longitudinal axis*. Journal of Applied Fluid Mechanics* 7(3), 435-446.

Taylor, G., R. Nudds and A. Thomas (2003). Flying and swimming animals cruise at a Strouhal number tuned for high power efficiency. *Letters to Nature* 425(6959), 707-711.

Triantafyllou, G. S., M. S. Triantafyllou and M. A. Grosenbaugh (1993). Optimal thrust development in oscillating foils with application to fish propulsion. *Fluids and Structures* 7(2), 205-224.

Vazquez, J. G. V. (2007). *Nonlinear Analysis of Orthotropic Membrane and Shell Structures Including Fluid-Structure Interaction.* Ph. D. thesis, Universitat politecnica de catalunya, Barcelona, Spain.

Wall, W. A. and E. Ramm (1998). Fluid-structure interaction based upon a stabilized (ale) finite element method. In *Proceeding of IV World Congress on Computational Mechanics*, Barcelona.

Wright, J. R. and J. E. Cooper (2007). *Introduction to Aircraft Aeroelasticity and Loads*. John Wiley and Sons.

Zhu, Q. (2007). Numerical simulation of a flapping foil with chordwise or spanwise flexibility. *AIAA* 45(10), 2448-2457.